Fabrication and Characterization of Nanopore-Based Electrodes with Radii down to 2 nm

Diego Krapf, Meng-Yue Wu, Ralph M. M. Smeets, Henny W. Zandbergen, Cees Dekker, and Serge G. Lemay*

Kavli Institute of Nanoscience, Delft University of Technology, Lorentzweg 1, 2628 CJ Delft, The Netherlands

ABSTRACT

We report on the fabrication and characterization of gold nanoelectrodes with carefully controlled nanometer dimensions in a matrix of insulating silicon nitride. A focused electron beam was employed to drill nanopores in a thin silicon nitride membrane. The size and shape of the nanopores were studied with high-resolution transmission electron microscopy and electron-energy-loss two-dimensional maps. The pores were subsequently filled with gold, yielding conically shaped nanoelectrodes. The nanoelectrodes were examined by atomic and electrostatic force microscopy. Their applicability in electrochemistry was demonstrated by steady-state cyclic voltammetry. Pores with a radii down to 0.4 nm and electrodes with radii down to 2 nm are demonstrated.

The ability to fabricate electrodes of accurately controlled nanometer dimensions is a key element in several areas of nanoscience, including molecular electronics and nanoelectrochemistry. Point contacts have been used widely in quantum transport studies[1,2] and to probe electrical conduction through a limited number of molecules down to the single-molecule level.[3−6] In the context of electrochemistry, the main fundamental interest in these devices lies in their unique properties for the study of electron-transfer kinetics[7,8] and mass-transport mechanisms in localized nanometer-scale volumes.[9−11] In general, as the size of an electrode is reduced, it is possible to obtain higher sensitivity, a lower detection limit, a smaller volume probed, and higher temporal resolution. Hence, metal nanoelectrodes are used in liquids in a broad spectrum of applications such as single-molecule detection,[12] probing neurophysiological signals of small populations,[13,14] biomolecular sensors for medical diagnostics,[15] and real-time monitoring of cell exocytosis.[16]

The most common approach for electrode fabrication consists of electrochemically etching a thin wire down to a sharp conical shape followed by insulating the whole surface except for the very apex of the tip. The most broadly used insulating materials include electrophoretic paint[17,18] and Apiezon wax.[8,19] Another preparation technique consists of stretching glass capillaries containing sealed microwires with a laser micropipet puller.[20,21] Despite their large potential applicability, major obstacles still have to be overcome for the wider use of nanoelectrodes. In particular, the long-term instability and the difficulty in characterizing the size and shape of present-state nanoelectrodes lead to significant uncertainties in the analysis of experimental results.

Here we report a novel method for the fabrication of metallic nanoelectrodes with carefully controlled dimensions of a few nm. We particularly focus on gold nanoelectrodes, although the extension of this process to other metals is straightforward. Our method consists of drilling a nanopore in a silicon nitride membrane using a focused electron beam, a method developed recently for nanofluidic applications.[22−24] We then fill the pore with an evaporated noble metal to yield conically shaped protruding electrodes. We present the characterization of these nanoelectrodes and demonstrate their applicability in electrochemical voltammetry.

Nanoelectrodes were fabricated by drilling nanometer-scale pores in a thin SiN membrane and subsequently filling the nanopores with gold. A schematic representation of the desired electrode geometry is presented in Figure 1, and the fabrication process is outlined in Figure 2. The SiN membranes were manufactured following standard microfabrication technology from the semiconductor industry. Boron-doped Si (100) wafers with resistivities of 20−30 Ω cm were used. First, a three-layer structure was deposited by low-pressure chemical vapor deposition (LPCVD) on both sides as follows: 20 nm of low-stress (silicon-rich) SiN, followed by 200 nm of SiO_2 and a 500-nm thick capping layer of low-stress SiN. The middle SiO_2 layer was deposited from tetraethoxysilane (TEOS). Square windows were then pat-

* Corresponding author: Fax: +31-15-2781202; e-mail: lemay@ mb.tn.tudelft.nl.
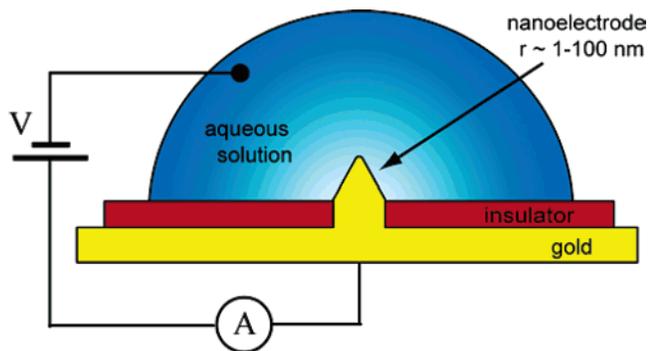
Figure 1. Schematic representation of a nanopore-based electrode in a typical electrochemical experiment.
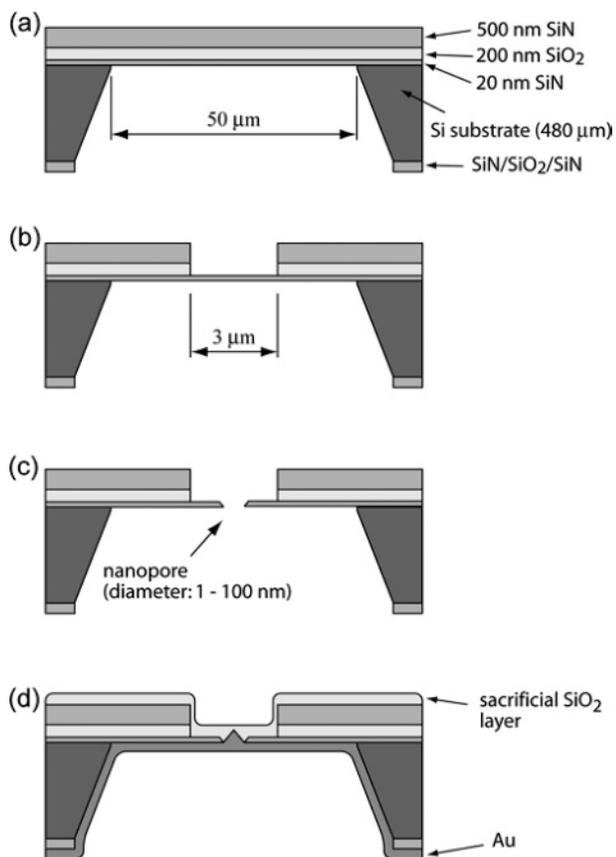
Figure 2. Main steps of the nanoelectrode fabrication process. (a) CVD three-layer deposition on Si, backside lithography, and KOH etch. (b) Front-side lithography and etch of the SiN and SiO_2 layers forming a 20-nm SiN free-standing membrane. (c) Nanopore drilling in the SiN membrane with a focused electron beam. (d) Sacrificial SiO_2 layer sputtering and Au evaporation. After this step, the sacrificial layer is removed in buffered HF.

terned in poly(methyl methacrylate) (PMMA) on the backside of the wafer with e-beam lithography, and the pattern was transferred to the CVD layers with CHF_3/O_2 reactive ion etching (RIE) at 8 μbar (CHF_3 50, O_2 2.5 sccm, 50 W, etching time ~60 min). Using the SiN as a mask, the Si substrate was anisotropically etched in KOH (30 wt. %, 80 °C, etching time ~8 h), yielding free-standing 50 × 50 μm^2 membranes consisting of the three-layer stack (Figure 2a). To reveal the lowermost 20-nm SiN film, circular windows, 3 μm in diameter, were patterned in PMMA with e-beam

lithography on the front side of the samples in the middle of the 50-μm membranes. Inside these regions, the capping SiN and SiO_2 layers were removed with CHF_3/O_2 RIE and buffered HF etch, respectively (Figure 2b). Our membrane structure has two advantages over single-layer membranes. First, the capacitance of the membrane is greatly reduced because the 20-nm thickness has an area of only 7 μm^2, whereas the rest of the substrate is covered with an insulator thickness greater than 700 nm. Second, the mechanical strength is enhanced by the circular shape because the strain is homogeneously spread, in contrast to square-shaped membranes.

Pores with radii between 0.4 and 100 nm were obtained in the thin membranes with a focused electron beam[23,25] using a transmission electron microscope (TEM, Figure 2c). Pores with radii in the range of 1.5−4 nm were drilled directly with the electron beam. Here, an electron beam was tightly focused on the SiN membrane to an intensity of 10^8-10^9 e/nm^2 s. The high intensity of the electron beam breaks the covalent bonds and causes Si and N atoms to be sputtered away into the vacuum.[25] The time for pore formation can vary greatly depending on the beam parameters, ranging from less than 10 s for a 300 keV beam at ~10^9 e/nm^{2}s to 5 min for a 200 keV beam at ~10^8 e/nm^{2}s. To obtain bigger pores, a pore 2.5−4 nm in radius was drilled first and this pore was then expanded by broadening the electron beam (with an accompanying drop in intensity to values between 10^6 and 10^7 e/nm^{2}s). The pore growth was followed in real time by TEM imaging. When the pore achieved the desired size, the expanding process was stopped by decreasing the beam intensity substantially to less than 10^4 e/nm^{2}s. Pores with radii smaller than 1.5 nm were obtained in a related manner. Here a 1.5 nm pore was drilled and a low-intensity (10^5- 10^6 e/nm^{2}s) electron beam was then used to shrink this pore. Expansion and shrinkage are thought to be driven by surface-tension effects.[23] After pore formation, high-resolution transmission electron microscopy (HR-TEM) images were obtained in order to measure the pore diameter with high accuracy. This diameter determines the eventual electrode diameter.

We have found previously[26] that sputtering Au to cover one side of a pore results in an inverted pyramid geometry with typical sidewall angles of 60°. To obtain a convex electrode, a more sophisticated recipe was followed. A 0.5-nm Cr adhesion layer was evaporated at 10^{-7} Torr on the backside of the membrane followed by a 0.5-nm layer of Au without breaking the vacuum. The sample was then turned over and the front side of the pore was covered with SiO_2 by sputtering in an Ar plasma at 1 mTorr (power 100 W, rate 1 nm/min). An SiO_2 pit structure similar to those of ref 26 was obtained. This pit was subsequently filled with Au by a second backside evaporation (Figure 2d). To guarantee coverage of the pore, both the SiO_2 and Au layer thicknesses were at least 2.5 times the diameter of the pore. Finally, the front SiO_2 was removed in buffered HF to reveal a structure as depicted in Figure 1. All of the materials employed in the fabrication are compatible with the use of organic solvents such as acetone or trichloroethylene (TCE).
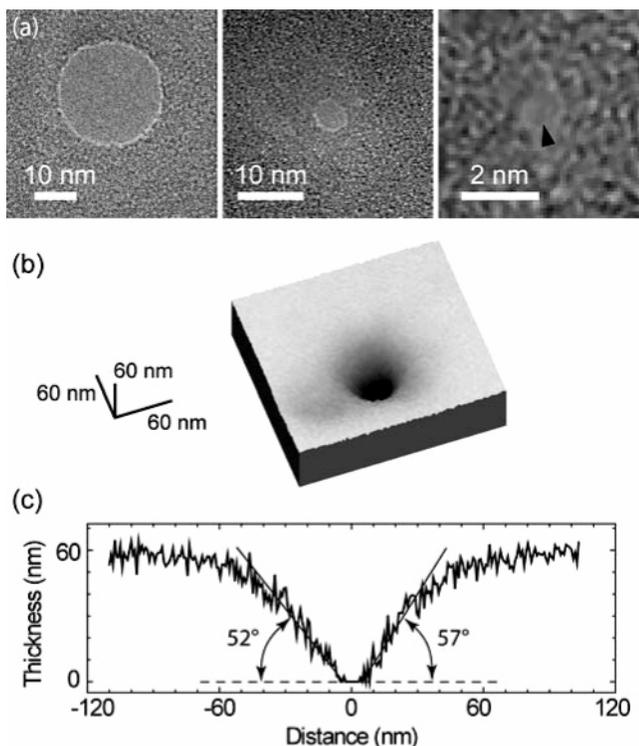
Figure 3. (a) HR-TEM images of nanopores with radii of 12, 2.5, and 0.4 nm. (b) Thickness map (smoothed) of a 3-nm-radius pore obtained with EELS. (c) Cross section of the pore thickness profile (raw data) passing through the pore in b. The absolute thickness was obtained by calibrating the relative thickness far from the pore to 60 nm.

Therefore, it is possible to chemically clean the electrodes if needed and to use them in nonaqueous solvents.

Figure 3a shows three different pores imaged with HR-TEM. Their radii are 12, 2.5, and 0.4 nm. The pore with a 2.5-nm radius was imaged right after formation by drilling with the focused beam. The 12-nm pore was first drilled and then expanded slowly in a controlled manner until this radius was achieved, whereas the pore with a 0.4-nm radius was formed by shrinking a pore with initial radius of about 1.5 nm. The pores have a well-defined circular shape and their diameter, which is readily measurable with very high accuracy, can correspondingly be controlled to subnanometer precision. Note that the smallest pore has a diameter spanning only five atoms.

To get some insight into the shape of the pores, we mapped their structure using electron-energy-loss spectroscopy (EELS). The local membrane thickness is determined by the log-ratio image of an energy-unfiltered and an energy-filtered image (with zero loss beam).[25,27] Because the EELS images acquired from a 20-nm-thick membrane were quite noisy, it was not possible to obtain quantitative information from these data. We instead obtained thickness maps of pores drilled in thicker membranes. These were prepared by covering both sides of the SiN membranes with 20-nm sputtered SiO_2 and drilling the pores into these 60-nm membranes. Figure 3b shows the thickness variation around a pore 6 nm in diameter created in 15 min using an electron beam diameter of 8 nm (full width at half-maximum). A three-dimensional recon-

struction of a thickness map and a cross section across the pore are shown. The region over which the thickness of the thin film varies extends much further (radius about 80 nm) than the radius of the beam. This implies that rearrangement of material occurs in the 80-nm radius area even though this material is not strongly exposed to the electron beam. Because material is not observed to accumulate outside the 80-nm-radius area, we believe that this material migrates to the central area, where it is sputtered away into the vacuum by the intense electron beam. From Figure 3b and c it is clear that the material around the pore has a wedge shape and forms sidewall angles of ~55°. EELS characterization of different pores indicates that this slope can span a range 30−60° depending on the electron-beam intensity and the duration of the drilling process. The radius of curvature at the constriction point is much smaller than the membrane thickness. We estimate an upper limit of 5 nm for the radius of curvature. Although some differences may exist between these kind of membranes and 20-nm SiN membranes, we expect that a wedge shape of the nanopores is a universal property of electron-beam drilling. Similar results were obtained in 40-nm SiN membranes.[25]

The fabricated nanoelectrodes were characterized by atomic force microscopy (AFM) and simultaneously with electrostatic force microscopy (EFM). In the latter technique, each line of the image was first scanned in tapping mode, and then a second interleave scan was performed along the same line. During the interleave scan, the electrically grounded tip was raised 50 nm and it was constrained to follow the measured topography while a voltage of 2 V was applied to the substrate. Because the atomic forces are very short-ranged, the tip only couples to long-range Coulomb interactions during the interleave scan. Electric field gradients are probed by recording the phase change of the cantilever oscillation. Because EFM is a direct probe of the electric field, it is an ideal tool to locally distinguish conductive and insulating regions in the sample. An AFM topographic image showing a conical electrode is presented in Figure 4a. The corresponding EFM image shown in Figure 4b confirms that the observed conical feature consists of metal surrounded by insulating material. The electrode presented in this figure has a radius (measured in TEM) of 24 nm. A topographic profile passing through the electrode is shown in Figure 4c. The wedge shape of the nanopores is apparent beside the nanoelectrode. Consistently with the expected geometrical shape, we measure a height of 30 nm from the SiN membrane to the tip of the electrode. The apparent radius of the electrode in AFM topography is 45 nm, but this is an upper limit only, because of the tip convolution. Unfortunately, the smallest electrodes could not be resolved with AFM because of the wedge shape of the nanopores (Figure 3c) combined with tip convolution.

We demonstrate the performance of the fabricated nanoelectrodes by probing their voltammetric response to redox couples. Ferrocenylmethyltrimethylammonium (FcTMA+) and ferrocenedimethanol (Fc(CH$_2$OH)$_2$) were employed as electroactive species and NH$_4$NO$_3$ was used as an inert base electrolyte. Ferrocenylmethyltrimethylammonium hexa-
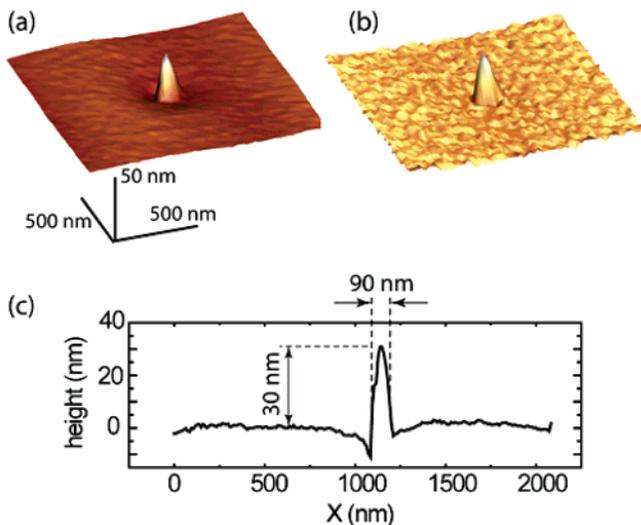
Figure 4. (a) AFM topography image of a nanoelectrode. (b) EFM image of the same electrode. (c) Cross section of the topographic image passing through the pore.

Figure 5. Cyclic voltammograms obtained for different electrodes recorded in solutions of (a) $Fc(CH_2OH)_2$ and (b) $FcTMA^+$. In the last curve, it is possible to see an enhancement of the noise in the regime where faradaic currents are recorded.[11] The voltammogram scan rates are (a) 10 mV/s, (b, top) 0.5 mV/s, and (b, bottom) 0.1 mV/s.

fluorophosphate was synthesized by metathesis of the iodide salt (Lancaster, England) with ammonium hexafluorophosphate (Aldrich).[26] Ammonium nitrate (Merck, Germany) and $Fc(CH_2OH)_2$ (Aldrich) were used as received. Aqueous solutions were prepared with 18 MΩ cm water from a Milli-Q purification system (Millipore, USA). Electrochemical measurements were performed in a 200 μL poly-(dimethylsiloxane) (PDMS) cell. The cell had two openings: a bottom one, 150 μm in diameter, that contacted the nanoelectrode and a macroscopic upper hole where a commercial Ag/AgCl electrode was placed as both the reference and counter electrode. The oxidation of the redox species in the presence of 0.5 M NH_4NO_3 was recorded in a two-electrode configuration using home-built electronics with a bandwidth of 3 Hz. At this salt concentration, the Debye length is roughly 0.4 nm. The electroactive species concentrations in the solutions were determined from the voltammetric limiting current measured at 10-μm disk electrodes (BASi).

Typical steady-state cyclic voltammograms are shown in Figure 5. The observed sigmoidal shape of the current−voltage curves provides a signature of the good performance of the electrode surface. In addition to the transport-limited faradaic currents, a hysteretic offset is measured between the forward and backward scans, resulting from the parasitic dielectric response of the insulating membrane. This is especially clear for the smallest electrodes where the faradaic currents are in the sub-pA levels. It should be noted that this nonfaradaic current is not the result of the metal-electrolyte double-layer capacitance. Instead, it is the effect of a dielectric relaxation of the membrane material.[28,29] The transport-limited currents achieved for the neutral species $Fc(CH_2OH)_2$ are in good agreement with the expected diffusion-limited current.[30] For example, the bottom voltammogram shown in Figure 5a displays a diffusion-limited plateau, $i_L = (5.2 \pm 0.2)$ pA. We can extract from this current an effective radius, $R_{eff} = (6.6 \pm 0.6)$ nm, in very good agreement with the measured radius, $R_0 = 6.5$ nm. Here R_{eff}

is defined from the diffusion-limited current at a hemispherical electrode $i_L = 2\pi FDCR_{eff}$, where F, D, and C are the Faraday constant, the diffusion coefficient, and the bulk concentration, respectively. However, interesting deviations from the classical picture are observed in the case of the positively charged species $FcTMA^+$. This anomalous transport behavior will be discussed elsewhere.[11]

A strong advantage of these kinds of electrodes is that their size can be characterized independently prior to their use without risking contamination of the metal surface. Our fabricated electrodes proved to be stable over long measuring periods. The voltammetric currents did not change over 36 h of continuous measurements. A drawback is their inability to probe high temporal resolutions because of the slow response of the insulating material surrounding them. This problem may be solved in the future by the use of a metallic guard layer set at the same potential as the electrode itself so that no potential drop is present across the dielectric membrane. Another simple way to avoid the slow dielectric response of the SiN membrane consists of working with thick polymer membranes such as those used in the fabrication of track-etched nanopores.[24,31] However, the slow response of the dielectric material presents no restriction in applications where the potential of the electrode is held constant, for example, biomolecular sensing.

We have demonstrated a novel process for fabricating nanoelectrodes as small as 2 nm in radius. Pores as small as 0.4 nm in radius were achieved using electron-beam drilling. The ultimate limiting factor in drilling small pores is the TEM resolution. We do not foresee any reason for limiting the use of these pores to obtain sub-1-nm gold electrodes.

References

(1) Ralls, K. S.; Buhrman, R. A. *Phys. Rev. Lett.* **1998**, *60*, 2434.
(2) Ralph, D. C.; Buhrman, R. A. *Phys. Rev. Lett.* **1992**, *69*, 2118.

(3) Andres, R. P.; Bein, T.; Dorogi, M.; Feng, S.; Henderson, J. I.; Kubiak, C. P.; Mahoney, W.; Osifchin, R. G.; Reifenberger, R. *Science* **1996**, *272*, 1323.

(4) Reed, M. A.; Zhou, C.; Muller, C. J.; Burgin, T. P.; Tour, J. M. *Science* **1997**, *278*, 252.

(5) Chen, J.; Reed, M. A.; Rawlett, A. M.; Tour, J. M. *Science* **1999**, *286*, 1550.

(6) Dadosh, T.; Gordin, Y.; Krahne, R.; Khivrich, I.; Mahalu, D.; Frydman V.; Sperling, J.; Yacoby, A.; Bar-Joseph, I. *Nature (London)* **2005**, *436*, 677.

(7) Penner, R. M.; Heben, M. J.; Longin, T. L.; Lewis, N. S. *Science* **1990**, *25*, 1118.

(8) Watkins, J. J.; Chen, J.; White, H. S.; Abruña, H. D. *Anal. Chem.* **2002**, *75*, 3962.

(9) Chen, S.; Kucernak, A. *Electrochem. Commun.* **2002**, *3*, 80.

(10) Watkins, J. J.; White, H. S. *Langmuir* **2004**, *20*, 5474.

(11) Krapf, D.; Wu, M. Y.; Quinn, B.; Zandbergen, H. W.; Dekker, C.; Lemay, S. G. In preparation.

(12) Fan, F. R. F.; Bard, A. J. *Science* **1995**, *267*, 871.

(13) Loeb, G. E.; Peck, R. A.; Martyniuk, J. *J. Neurosci. Methods* **1995**, *63*, 175.

(14) Qiao, Y.; Chen, J.; Guo, X.; Cantrell, D.; Ruoff, R.; Troy, J. *Nanotechnology* **2005**, *16*, 1598.

(15) Delvaux, M.; Demoustier-Champagne, S.; Walcarius, A. *Electro-analysis* **2004**, *16*, 190.

(16) Wu, W.; Huang, W. H.; Wang, W.; Wang, Z. L.; Cheng, J. K.; Xu, T.; Zhang, R. Y.; Chen, Y.; Liut, J. *J. Am. Chem. Soc.* **2005**, *127*, 8914.

(17) Bach, C. E.; Nichols, R. J.; Beckmann, W.; Meyer, H.; Schulte, A.; Besenhard, J. O.; Jannakoudakis, P. D. *J. Electrochem. Soc.* **1993**, *140*, 1281.

(18) Slevin, C. J.; Gray, N. J.; Macpherson, J. V.; Webb, M. A.; Unwin, P. R. *Electrochem. Commun.* **1999**, *1*, 282.

(19) Nagahara, L. A.; Thundat, T.; Lindsay, S. M. *Rev. Sci. Instrum.* **1989**, *60*, 3128.

(20) Shao, Y.; Mirkin, M. V.; Fish, G.; Kokotov, S.; Palanker, D.; Lewis, A. *Anal. Chem.* **1997**, *69*, 1627.

(21) Ballesteros Katemann, B.; Schuhmann, W. *Electroanalysis* **2002**, *14*, 22.

(22) Li, J.; Stein, D.; McMullan, C.; Branton, D.; Aziz, M. J.; Golovchenko, J. A. *Nature (London)* **2001**, *412*, 166.

(23) Storm, A. J.; Chen, J. H.; Ling, X. S.; Zandbergen, H. W.; Dekker, C. *Nat. Mater.* **2003**, *2*, 537.

(24) (a) Apel, P.; Korchev, Y. E.; Siwy, Z.; Spohr, R.; Yoshida, M. *Nucl. Instrum. Methods B* **2001**, *184*, 337. (b) Siwy, Z.; Fulinski, A. *Phys. Rev. Lett.* **2002**, *89*, 198103.

(25) Wu, M. Y.; Krapf, D.; Zandbergen, M.; Zandbergen, H.; Batson, P. E. *Appl. Phys. Lett.* **2005**, *87*, 113106.

(26) Lemay, S. G.; van der Broek, D. M.; Storm, A. J.; Krapf, D.; Smeets, R. M. M.; Heering, H. A.; Dekker, C. *Anal. Chem.* **2005**, *77*, 1911.

(27) Malis, T.; Cheng, S. C.; Egerton, R. F. *J. Electron Microsc. Tech.* **1988**, *8*, 193.

(28) Jonscher, A. K. *Nature (London)* **1977**, *267*, 673.

(29) Westerlund, S.; Ekstam, L. *IEEE Trans. Dielectr. Electr. Insul.* **1994**, *1*, 826.

(30) Bard, A. J.; Faulkner, L. R. *Electrochemical Methods: Fundamentals and Applications*, 2nd ed.; Wiley: New York, 2001.

(31) Enculescu, I.; Siwy, Z.; Dobrev, D.; Trautmann, C.; Toimil Molares, M. E.; Neumann, R.; Hjort, K.; Westerberg, L.; Spohr, R. *Appl. Phys. A* **2003**, *77*, 751.

NL052163X